

Unbalanced Regularized Optimal Mass Transport with Applications to Fluid Flows in the Brain

1st Xinan Chen

Department of Applied Mathematics
and Statistics
Stony Brook University
Stony Brook, NY, USA
xinan.chen@stonybrook.edu

2nd Helene Benveniste

Department of Anesthesiology
Yale School of Medicine
New Haven, CT, USA
helene.benveniste@yale.edu

3rd Allen Tannenbaum

Department of Applied Mathematics
and Statistics,
Department of Computer Science
Stony Brook University
Stony Brook, NY, USA
allen.tannenbaum@stonybrook.edu

Abstract—Generalizing the fluid dynamical optimal mass transport (OMT) approach of Benamou and Brenier, *regularized optimal mass transport* (rOMT) formulates a transport problem from an initial mass configuration to another with the optimality defined by the kinetic energy, but subject to an advection-diffusion constraint equation. Both rOMT and the Benamou and Brenier’s formulation require the total initial and final masses to be equal; mass is preserved during the entire transport process. However, for many applications, e.g., in dynamic image tracking, this constraint is rarely if ever satisfied. We introduce an unbalanced version of rOMT to remove this constraint together with a detailed numerical solution procedure and applications to dynamic image tracking in the brain.

Index Terms—regularized optimal mass transport, unbalanced optimal transport, computational fluid dynamics

I. INTRODUCTION

Optimal mass transport (OMT) is concerned with finding the transport mapping from an initial mass distribution to a final one, with optimality defined relative to a given convex cost functional [10], [14]–[16]. A dynamic formulation of the OMT problem was proposed by Benamou and Brenier [2] using the L^2 distance as the cost functional, whose formal description is as follows. Given the initial mass distribution function $\rho_0(x) \geq 0$ and the final one $\rho_1(x) \geq 0$ defined on bounded space $\Omega \subseteq \mathbb{R}^3$, the OMT problem is equivalent to solving

$$\min_{\rho, v} \int_0^T \int_{\Omega} \|v(t, x)\|^2 \rho(t, x) dx dt \quad (1a)$$

$$\text{subject to } \frac{\partial \rho}{\partial t} + \nabla \cdot (\rho v) = 0, \quad (1b)$$

$$\rho(0, x) = \rho_0(x), \quad \rho(T, x) = \rho_1(x) \quad (1c)$$

where a temporal dimension $t \in [0, T]$ is added to the transport process. In the above expression, $\rho(t, x)$ is the dynamic density function, and $v(t, x)$ is the velocity field defining the flow from ρ_0 to ρ_1 . Equation (1b) is called the *continuity equation* in fluid dynamics, and characterizes the advective transport of a conserved quantity. As an extension of model (1a)–(1c), a regularized version of OMT (rOMT) has been developed and applied in various places in which one includes a diffusive motion into the transport; see [5], [8], [11] and the many references therein. More precisely, a diffusion term is

added into the continuity equation (1b) in the dynamic OMT problem:

$$\frac{\partial \rho}{\partial t} + \nabla \cdot (\rho v) = \sigma \Delta \rho, \quad (2)$$

where the constant $\sigma > 0$ is the diffusion coefficient. Equation (2) is thus an *advection-diffusion equation*. The rOMT model has been proven useful for a number of important tracking problems in computational fluid dynamics (CFD), such as in quantifying and visualizing the movement of solutes in the brain [3], [4].

As is well-known, both the OMT and rOMT models must satisfy the mass conservation constraint, namely $\int_{\Omega} \rho_0(x) dx = \int_{\Omega} \rho_1(x) dx$. Indeed as formulated in (2), neither advection nor diffusion will change the total mass locally or globally in the given domain Ω . However, for applications in dynamic imagery in which either OMT or rOMT is employed as an optical flow tracking method, this is almost never the case. For example, in Dynamic Contrast Enhanced MRI (DCE-MRI) data, an early climbing period of total image intensity is usually observed, since it takes time for tracers to reach and fill the region of interest. Under these circumstances, if we assume the intensity of image signal is proportional to the density and mass in the model, the mass conservation law is no longer satisfied and thus the OMT and rOMT models cannot be directly applied. Nevertheless, analyzing the initial accumulating stage of tracers may help uncover interesting transport patterns and therefore a new model is necessary.

In the present work, we introduce the *unbalanced regularized OMT* (urOMT) model where a new independent variable and its indicator function are added as a sink or source of mass. The urOMT problem is formulated as follows:

$$\min_{\rho, v, r} \int_0^T \int_{\Omega} (\|v(t, x)\|^2 \rho(t, x) + \alpha \chi(t, x) r(t, x)^2 \rho(t, x)) dx dt \quad (3a)$$

$$\text{subject to } \frac{\partial \rho}{\partial t} + \nabla \cdot (\rho v) = \sigma \Delta \rho + \chi \rho r, \quad (3b)$$

$$\rho(0, x) = \rho_0(x), \quad \rho(T, x) = \rho_1(x) \quad (3c)$$

where $r(t, x)$ is the relative source variable, $\chi(t, x)$ is the given indicator function of $r(t, x)$ which takes values either 0 or 1 to constrain r to a certain spatial and temporal location, and

$\alpha > 0$ is the weighting parameter of the source term in the cost functional. This model takes inputs $\rho_0(x)$ and $\rho_1(x)$, and solves for the optimal $\rho(t, x)$, $v(t, x)$ and $r(t, x)$. We should note that we prefer to use the relative source r which controls the rate of mass creation ($r > 0$) and disappearance ($r < 0$), rather than $s = \rho r$, since the resulting expressions are cleaner. Even though r plays a role as a sink of mass when $r < 0$ and a role as a source of mass when $r > 0$, in our work we call r as the relative “source” to broadly refer to its ability to generate unbalanced mass instantaneously. One can imagine that r is the source of both positive and negative mass. The main point is that we no longer require the mass conservation condition for the input images ρ_0 and ρ_1 .

The unbalanced OMT problem has been studied both theoretically and with various applications including to imaging and shape deformation; see [1], [6], [7], [9], [12], [13] and the references therein.

Briefly summarizing the present paper, in Section II, we give the detailed numerical method for the urOMT model, while in Section III, we show results of some of the applications to fluid dynamical tracking.

II. NUMERICAL METHOD

In this section, we elaborate on the numerical method developed for the urOMT problem (3a)-(3c) on 3D data, especially on images in which intensity levels are assumed to represent the concentration of tracers, and are therefore proportional to mass/density in our model. Note that this method can be easily adapted to densities in any dimension.

A. Model

Given a pair of 3D images, $\rho_0^{img}(x)$ and $\rho_1^{img}(x)$, and indicator $\chi(x, t)$, in order to account for image noise, we consider posing a free end-point problem, so that we can remove the constraint $\rho(T, x) = \rho_1^{img}(x)$. Another fitting term is consequently added into the cost function. The model we solve is therefore written as:

$$\min_{v, r} \int_0^T \int_{\Omega} \rho(t, x) (\|v(t, x)\|^2 + \alpha \chi(t, x) r(t, x)^2) dx dt + \beta \int_{\Omega} (\rho(T, x) - \rho_1^{img}(x))^2 dx \quad (4a)$$

$$\text{subject to } \frac{\partial \rho}{\partial t} + \nabla \cdot (\rho v) = \sigma \Delta \rho + \chi \rho r, \quad (4b)$$

$$\rho(0, x) = \rho_0^{img}(x), \quad (4c)$$

where $\beta > 0$ is the weighing parameter for the fitting term in the cost function. The dynamic density function $\rho(t, x)$ can be derived starting at ρ_0^{img} following equation (4b) with a velocity field v and a relative source r , so ρ is removed from the optimized variables. Basically, in this set-up ρ becomes a *state variable*. We call this model the *unbalanced regularized OMT with free end-point* (free-urOMT).

B. Discretization

Since 3D images are typically defined on cubical domains, we divide the space Ω into a cell-centered grid of size $n_1 \times n_2 \times n_3$ with uniform voxel length Δx . Let $n = n_1 n_2 n_3$ be the total number of voxels. The time interval $[0, T]$ is partitioned into m equal sub-intervals with length $\Delta t = \frac{T}{m}$. Then we have $m + 1$ discrete time steps $t_i = i \Delta t$ for $i = 0, \dots, m$. The density function $\rho(t, x)$ may be discretized into ρ_i for $i = 0, \dots, m$, each denoting the mass distribution at t_i , and where $\rho_0 = \rho_0^{img}$ denotes the given initial image. The velocity field $v(t, x)$, relative source $r(t, x)$ and its indicator $\chi(t, x)$ may also be discretized into v_i , r_i and χ_i for $i = 0, \dots, m-1$, each denoting the velocity field, relative source change, and the indicator transforming ρ_i to ρ_{i+1} , respectively. Note that we refer to all ρ_i, v_i, r_i and χ_i by their vector form. We further denote $\rho = [\rho_1; \dots; \rho_m]$, $v = [v_0; \dots; v_{m-1}]$, $r = [r_0; \dots; r_{m-1}]$ and $\chi = [\chi_0; \dots; \chi_{m-1}]$.

So far, we have defined the discretized variables on the space and time grids. The cost function equation (4a) may be therefore approximated by

$$\Gamma = \Gamma_1 + \alpha \Gamma_2 + \beta \Gamma_3 \quad (5)$$

where

$$\Gamma_1 = \Delta t (\Delta x)^3 \rho^T (I_m \otimes [I_n | I_n | I_n]) (v \odot v), \quad (6a)$$

$$\Gamma_2 = \Delta t (\Delta x)^3 \rho^T (r \odot r \odot \chi), \quad (6b)$$

$$\Gamma_3 = \|\rho_m - \rho_1^{img}\|^2. \quad (6c)$$

Here \otimes denotes the Kronecker tensor product, and \odot denotes the Hadamard product. Further, $[\cdot]$ represents the block matrix, while $\|\cdot\|$ means taking the L^2 norm of a vector. I_k is the k -dimensional identity matrix for $k \in \mathbb{N}^+$.

Next, we deal with the partial differential equation (4b). We pose ghost points outside of the boundary and employ the Neumann boundary condition such that the derivative across boundary is always 0. The Laplacian operator Δ may be approximated with matrix Q under the aforementioned numerical grid and boundary condition. We use operator-splitting method to solve the equation. To be precise, at each time step from t_i to t_{i+1} for $i = 0, \dots, m-1$, we divide the whole process into first: mass creation/disappearance: $\frac{\partial \rho}{\partial t} = \chi \rho r$, second: advection: $\frac{\partial \rho}{\partial t} + \nabla \cdot (\rho v) = 0$ and third: diffusion: $\frac{\partial \rho}{\partial t} = \sigma \Delta \rho$. For the first mass creation/disappearance step, the equation may be discretized as

$$\frac{1}{\Delta t} (\rho_i^{src} - \rho_i) = \rho_i \odot r_i \odot \chi_i \quad (7a)$$

$$\Rightarrow \rho_i^{src} = (1_n + \Delta t \cdot r_i \odot \chi_i) \odot \rho_i \quad (7b)$$

where 1_n is a vector of length n consisting of 1. The second advection step is

$$\rho_i^{adv} = S(v_i) \rho_i^{src}, \quad (8)$$

where $S(v_i)$ is the averaging matrix with respect to v_i using the particle-in-cell method which redistributes transported mass to its nearest neighbors by a certain ratio. The (j, k) entry of $S(v_i)$ is the ratio of mass allocated from old location k to

new location j . By applying $S(v_i)$ to a vector which represents a mass distribution, we can derive a new mass distribution following the velocity v_i . The third diffusion step employs the Euler Backwards scheme in the following manner:

$$\begin{aligned} \frac{1}{\Delta t}(\rho_{i+1} - \rho_i^{adv}) &= \sigma Q \rho_{i+1} \quad (9a) \\ \Rightarrow (I_n - \sigma \Delta t \cdot Q) \rho_{i+1} &= \rho_i^{adv}. \quad (9b) \end{aligned}$$

Combining all three steps (7b), (8) and (9b), we have

$$(I_n - \sigma \Delta t \cdot Q) \rho_{i+1} = S(v_i)(1_n + \Delta t \cdot r_i \odot \chi_i) \odot \rho_i. \quad (10)$$

If we denote

$$L = I_n - \sigma \Delta t \cdot Q, \quad (11a)$$

$$R(r_i) = I_n + \Delta t \cdot \text{diag}(r_i \odot \chi_i), \quad (11b)$$

where $\text{diag}(\cdot)$ is the operator turning a vector into a diagonal matrix. Equation (10) may be re-written as $\rho_{i+1} = L^{-1}S(v_i)R(r_i)\rho_i$ for $i = 0, \dots, m-1$ where $S(v_i)$ and $R(r_i)$ are n -th dimensional matrix with respect to v_i and r_i , respectively. In conclusion, we have discretized the free-urOMT problem (4a)-(4c) as follows:

$$\min_{v,r} \quad \Gamma = \Gamma_1 + \alpha \Gamma_2 + \beta \Gamma_3 \quad (12a)$$

$$\text{subject to} \quad \rho_{i+1} = L^{-1}S(v_i)R(r_i)\rho_i, \text{ for } i = 0, \dots, m-1, \quad (12b)$$

$$\rho_0 = \rho_0^{img}, \quad (12c)$$

where Γ_1, Γ_2 and Γ_3 are explicitly given in (6a)-(6c).

C. Gradient and Hessian

Notice that in the discrete problem (12a)-(12c), the cost function is quadratic and the constraints are linear with respect to the variables v and r . With given v and r , we can derive ρ and ρ_m in the cost function (12a) with the differential equation constraint (12b). We therefore use the Gauss-Newton method to optimize the problem. This involves computing the gradient and Hessian matrix of Γ for variables v and r . Next, we focus on calculating the gradient of Γ : $g = [g_v; g_r]$ where $g_v = \frac{\partial \Gamma}{\partial v}$ and $g_r = \frac{\partial \Gamma}{\partial r}$, and the Hessian matrix of Γ : $H = [H_{11}, H_{12}; H_{21}, H_{22}]$ where $H_{11} = \frac{\partial^2 \Gamma}{\partial v^2}$, $H_{12} = \frac{\partial^2 \Gamma}{\partial v \partial r}$, $H_{21} = \frac{\partial^2 \Gamma}{\partial r \partial v}$ and $H_{22} = \frac{\partial^2 \Gamma}{\partial r^2}$.

Equation (12b) shows that ρ_k is determined by $v_0, \dots, v_{k-1}, r_0, \dots, r_{k-1}$ and is thus independent of v_j and r_j for $j \geq k$. Defining

$$J_{v_j}^k = \frac{\partial \rho_k}{\partial v_j}, \quad J_{r_j}^k = \frac{\partial \rho_k}{\partial r_j} \quad (13)$$

for $k = 1, \dots, m, j = 0, \dots, m-1$, then $J_{v_j}^k = 0$ and $J_{r_j}^k = 0$ always hold for $j \geq k$. If we further denote

$$J_v = \frac{\partial \rho}{\partial v} = (J_{v_j}^k)_{k,j}, \quad J_r = \frac{\partial \rho}{\partial r} = (J_{r_j}^k)_{k,j}, \quad (14)$$

then J_v and J_r are lower-triangular block matrices. Let $J_v^m = [J_{v_0}^m | J_{v_1}^m | \dots | J_{v_{m-1}}^m]$ denote the last row block of J_v and J_r^m for that of J_r . For the gradients, we have

$$g_v = \frac{\partial \Gamma_1}{\partial v} + \alpha \frac{\partial \Gamma_2}{\partial v} + \beta \frac{\partial \Gamma_3}{\partial v} \quad (15a)$$

$$\begin{aligned} &= \Delta t (\Delta x)^3 (2\rho^T M \text{diag}(v) + (M(v \odot v))^T J_v) \\ &\quad + \alpha \Delta t (\Delta x)^3 (r \odot r \odot \chi)^T J_v \\ &\quad + 2\beta (\rho_m - \rho_1^{img})^T J_v^m \end{aligned} \quad (15b)$$

$$g_r = \frac{\partial \Gamma_1}{\partial r} + \alpha \frac{\partial \Gamma_2}{\partial r} + \beta \frac{\partial \Gamma_3}{\partial r} \quad (16a)$$

$$\begin{aligned} &= \Delta t (\Delta x)^3 (M(v \odot v))^T J_r \\ &\quad + \alpha \Delta t (\Delta x)^3 (2\rho^T \text{diag}(r \odot \chi) + (r \odot r \odot \chi)^T J_r) \\ &\quad + 2\beta (\rho_m - \rho_1^{img})^T J_r^m \end{aligned} \quad (16b)$$

where we use $M = I_m \otimes [I_n | I_n | I_n]$ for simplicity of notation. To satisfy the symmetry of the Hessian matrix and to omit some complex second-order terms, we have

$$H_{11} \approx 2\Delta t (\Delta x)^3 \text{diag}(\rho^T M) + 2\beta (J_v^m)^T J_v^m \quad (17a)$$

$$H_{22} \approx 2\alpha \Delta t (\Delta x)^3 \text{diag}(\rho \odot \chi) + 2\beta (J_r^m)^T J_r^m \quad (17b)$$

$$H_{12} \approx 2\beta (J_v^m)^T J_r^m \quad (17c)$$

$$H_{21} \approx 2\beta (J_r^m)^T J_v^m \quad (17d)$$

As for the formulation of J_v^m and J_r^m , by the structure of (12b), we have that for $j = 0, \dots, m-1$,

$$J_{v_j}^m = L^{-1}S(v_{m-1})R(r_{m-1}) \dots L^{-1}S(v_{j+1})R(r_{j+1})L^{-1}B_j \quad (18)$$

where

$$B_j = \frac{\partial}{\partial v_j} (S(v_j)R(r_j)\rho_j) \quad (19)$$

is linear to v_j and

$$\begin{aligned} J_{r_j}^m &= \Delta t \cdot L^{-1}S(v_{m-1})R(r_{m-1}) \dots L^{-1}S(v_{j+1})R(r_{j+1}) \\ &\quad L^{-1}S(v_j) \text{diag}(\rho_j \odot \chi_j). \end{aligned} \quad (20)$$

J_v and J_r can be therefore computed recursively due to their lower-triangularity.

D. Algorithm

With the formulation of the gradient g and Hessian matrix H , we can utilize the Gauss-Newton Method to find the optimal solution. See Algorithm 1 for details. If we have more than two successive given images, $\rho_0^{img}, \rho_1^{img}, \dots, \rho_{q-1}^{img}$ and corresponding given indicator functions $\chi_0^{img}, \chi_1^{img}, \dots, \chi_{q-2}^{img}$ between adjacent images where $q > 2$ and $q \in \mathbb{N}^+$, we can run the algorithm iteratively by putting the last interpolated image ρ_m of the previous loop into the next loop as the initial image in order to derive smoother velocity fields.

The code is available at <https://github.com/xinan-nancy-chen/urOMT>.

Algorithm 1: Gauss-Newton Method

```

Load in  $\rho_0^{img}, \rho_1^{img}$  and  $\chi$ , and other parameters;
 $[v; r] = \text{initial guess}$ ;
for  $i = 1, 2, \dots, \text{MaxIter}$  do
    Compute interpolations from the partial differential
    equation:  $\rho = \text{SrcAdvDiff}(\rho_0^{img}, \chi, v, r)$ ;
    Compute gradient  $g$  and Hessian function handle  $Hx$ ;
    Solve linear system  $Hx = -g$  for  $x$ ;
    Do line search to find length  $l$ ;
    if line search fails then
        return  $[v; r]$ ;
    end if
    Update  $[v; r] = [v; r] + lx$ ;
end for
return  $[v; r]$ ;

```

III. RESULTS

In this section, we give some examples illustrating the urOMT methodology. Obviously, the model admits both the Eulerian and Lagrangian perspectives. The Eulerian formulation focuses on the fluid flow at fixed locations over time while the Lagrangian formulation enables one to follow the trajectory of a given particle over time and therefore analyze the features along the trajectory.

Specifically, suppose we run the urOMT algorithm on given $\rho_0^{img}, \rho_1^{img}, \dots, \rho_{q-1}^{img}$ and $\chi_0^{img}, \chi_1^{img}, \dots, \chi_{q-2}^{img}$ with discretization described in section II, the algorithm will run $q - 1$ successive loops and return the solutions

$$v_k^* = \begin{bmatrix} v_{k,0}^* \\ \vdots \\ v_{k,m-1}^* \end{bmatrix} \text{ and } r_k^* = \begin{bmatrix} r_{k,0}^* \\ \vdots \\ r_{k,m-1}^* \end{bmatrix} \quad (21)$$

for $k = 1, \dots, q - 1$ where the subscript k stands for the k -th loop. By taking the L^2 norm of $v_{k,0}^*, \dots, v_{k,m-1}^*$, we derive the optimal speed

$$s_k^* = \begin{bmatrix} s_{k,0}^* \\ \vdots \\ s_{k,m-1}^* \end{bmatrix} = \begin{bmatrix} \|v_{k,0}^*\| \\ \vdots \\ \|v_{k,m-1}^*\| \end{bmatrix}. \quad (22)$$

Therefore, $r_{k,i}^*$ and $s_{k,i}^*$ are called the *Eulerian relative-source maps* and *Eulerian speed maps*, respectively, for $k = 1, \dots, q - 1$ and $j = 0, \dots, m - 1$, and they allow us to observe the fluid flows at fixed coordinates at different discrete time steps. For ease of visualization, we define the *time-averaged Eulerian speed map* and *time-averaged Eulerian relative source map* between $\rho_{N_0}^{img}$ and $\rho_{N_1}^{img}$ as

$$\frac{1}{m(N_1 - N_0)} \sum_{k=N_0+1}^{N_1} \sum_{j=0}^{m-1} s_{k,j}^* \quad (23)$$

and

$$\frac{1}{m(N_1 - N_0)} \sum_{k=N_0+1}^{N_1} \sum_{j=0}^{m-1} r_{k,j}^*, \quad (24)$$

respectively, where $0 \leq N_0 < N_1 \leq q - 1$ and $N_0, N_1 \in \mathbb{N}^+$. In contrast, the post-processing framework developed in [3], [11] which follows Lagrangian coordinates can give the binary trajectories of the fluid flows which we call *pathlines* in our work. If we endow the pathlines with more information, for example, the speed (the L^2 norm of the velocity field) and the relative source, we can derive what we call *speed-lines* and *relative-source-lines*, respectively.

A. Gaussian Spheres

In this experiment, we created five successive 3D Gaussian spheres $\rho_0^{img}, \rho_1^{img}, \dots, \rho_4^{img}$ and put them into the urOMT algorithm. These spheres were created to gain more mass/intensity everywhere, be transported forward and then be diffused from the previous sphere (Figure 1a). In the k -th loop, the indicator function was set to 1 where $\rho_{k-1}^{img} + \rho_k^{img} > 10$ for all time steps to only allow mass gains and loss to occur in core regions, otherwise 0. The parameters are listed in Table I. The computation was completed on the Seawulf cluster with 40-core CPU which took about 100 minutes.

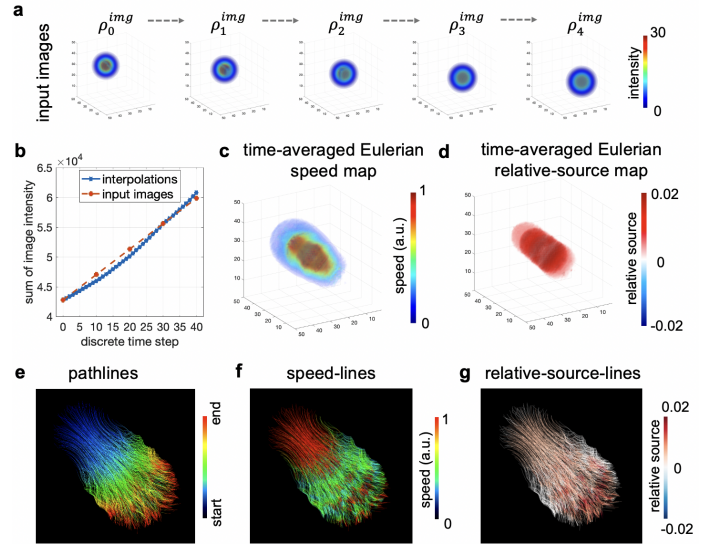


Fig. 1. 3D Gaussian Spheres: **a**: Five Gaussian spheres, shown in 3D rendering, were created as inputs to the urOMT algorithm. **b**: The total intensity of returned interpolations is compared to that of input images. **c-d**: Under Eulerian coordinates, the time-averaged speed map and relative-source map visualized in 3D rendering, indicate the speed and mass gains/loss distribution in the domain, respectively. **e-g**: Under Lagrangian coordinates, the binary trajectories of the transport are recorded by pathlines color-coded with starting and ending points. By endowing the pathlines with speed and relative source, we derive the speed-lines and relative-source-lines, respectively.

The total intensity of returned interpolations $\rho_{k,j}$ for $k = 1, \dots, 4$ and $j = 0, \dots, 9$ are compared to the total intensity of the five input images to ensure the Gaussian sphere is efficiently gaining mass/intensity over time through the optimal solutions (Figure 1b). From the Eulerian perspective, we show the time-averaged speed map and relative-source map between ρ_0^{img} and ρ_4^{img} (Figure 1c-d). The algorithm successfully captured the mass gains during the process and recognized

the core regions as of higher speed. With Lagrangian post-processing, we derived the pathlines, speed-lines and relative-source-lines under Lagrangian coordinates (Figure 1e-g). The pathlines exhibit what trajectories of particles look like over time, if they were put at given initial points in the system at $t = 0$. The funnel-shape of the pathlines are probably due to the accumulated effect of diffusion which disperses the mass. The speed-lines, pathlines endowed with speed, indicate that higher speed occurred mainly in the center of the spheres. The relative-source-lines show that mass was gained stably throughout the process with some zeros (color-coded with white) in the outer regions due the posing of indicator functions.

TABLE I
PARAMETERS USED IN UROMT ALGORITHM

Parameter	Definition	Value for Sphere Data	Value for Brain Data
n_1	grid size in x axis	50	100
n_2	grid size in y axis	50	106
n_3	grid size in z axis	50	100
q	number of input images	5	15
m	number of time intervals	10	
Δt	length of each time interval	0.4	
Δx	length of spatial grid	1	
σ	diffusion coefficient	0.002	
α	weighting parameter for the source term	10000	3000
β	weighting parameter for the fitting term	50	50
χ	indicator function of r	1 where initial + final images > 10	all 1's

B. Rat Brain MRI

In this experiment, our method was tested on the 3D DCE-MRI data derived from a 3-month-old healthy rat brain. Tracers, gadoteric acid, were injected into the cerebrospinal fluid (CSF) of the rat from the neck after the rat was anesthetized. The DCE-MRI data of the rat brain were collected every 5 minutes and lasted for 140 minutes, ending up with 29 images in total. The images were then processed to derive the % signal change from the baseline. More information of the data may be found in [3]. In this numerical experiment, we inputted every other image in order to save running time, which gave a total of 15 images: $\rho_0^{img}, \rho_1^{img}, \dots, \rho_{14}^{img}$ for the urOMT algorithm (Figure 2a). In [3], the rOMT model was applied right before the peak of the total signal intensity of the input images, i.e., $\rho_3^{img}, \dots, \rho_{14}^{img}$ in this case. In the present experiment, we were able to include earlier frames when the intensity was still rapidly increasing, due to the introduction of the relative source term in the model (Figure 2g orange curve). As no information is provided *a priori* for mass appearance and disappearance, we set the indicator function χ to be identically equal to 1. The parameters are listed in Table

I. The computation was completed on the Seawulf cluster with 28-core CPU, which took about 18.6 hours.

We show the time-averaged Eulerian relative-source maps and speed maps between every other input frame (Figure 2b-c). The Eulerian relative source shows that the tracers first entered the CSF sink of the brain causing the intensive mass gains therein, and then they subsequently moved into the deeper brain tissue causing the mass loss in CSF and mass gains in brain tissue. The Eulerian speed maps indicate that the speed of tracers actively entering CSF was very high in early times and then slowed down when tracers penetrated deeper, probably due to the physical resistance from the tissue. From the Lagrangian perspective, we show the pathlines of tracers starting at $t = 0$ and those lines endowed with speed and relative source (Figure 2d-f). The pathlines give the pathways/trajectories of tracers entering the CSF and brain tissue. The speed-lines show that higher speed was mainly along CSF base and large vessels. According to the relative-source-lines, tracers at $t = 0$ mainly underwent strong mass gains all the way through CSF to brain.

In urOMT model, the parameter α penalizes the source term in the cost function. In theory, as $\alpha \rightarrow +\infty$, r gets suppressed and this model approximates the rOMT model where unbalanced mass gains and loss are not allowed. In the above test, we used $\alpha = 3000$, and we further tested with $\alpha = 50000$ and plotted the total intensity curve of returned interpolations (Figure 2g). As illustrated, the interpolations from $\alpha = 3000$ gained extra mass in the early six frames and quickly lost mass later on, consistent with what the input images did. In contrast, the urOMT model with a much larger α (or the rOMT model) was incapable of capturing the correct mass gains and loss trend as r got over-penalized (or no source variable is included in the model).

IV. DISCUSSION

The urOMT methodology incorporates both advection and diffusion motions into the transport process, as well as allows mass to be created and destroyed in the dynamics by introducing a relative source variable. For special cases, it can also constrain the relative source to a given region or time interval. As an extension of rOMT model, urOMT model removes the mass conservation constraint, while keeping the attractive advection-diffusion framework, making it applicable to many real-world CFD modeling problems.

ACKNOWLEDGMENTS

This research was supported by AFOSR grants (FA9550-17-1-0435, FA9550-20-1-0029) and NIH grant (R01AT011419).

REFERENCES

- [1] Jean-David Benamou. Numerical resolution of an unbalanced mass transport problem. *ESAIM: Math. Model. Numer. Anal.*, 37(2):851–868, 2010.
- [2] Jean-David Benamou and Yann Brenier. A computational fluid mechanics solution to the monge-kantorovich mass transfer problem. *Numerische Mathematik*, 84(3):375–393, 2000.
- [3] Xinan Chen et al. Cerebral amyloid angiopathy is associated with glymphatic transport reduction and time-delayed solute drainage along the neck arteries. *Nature Aging*, 2022.

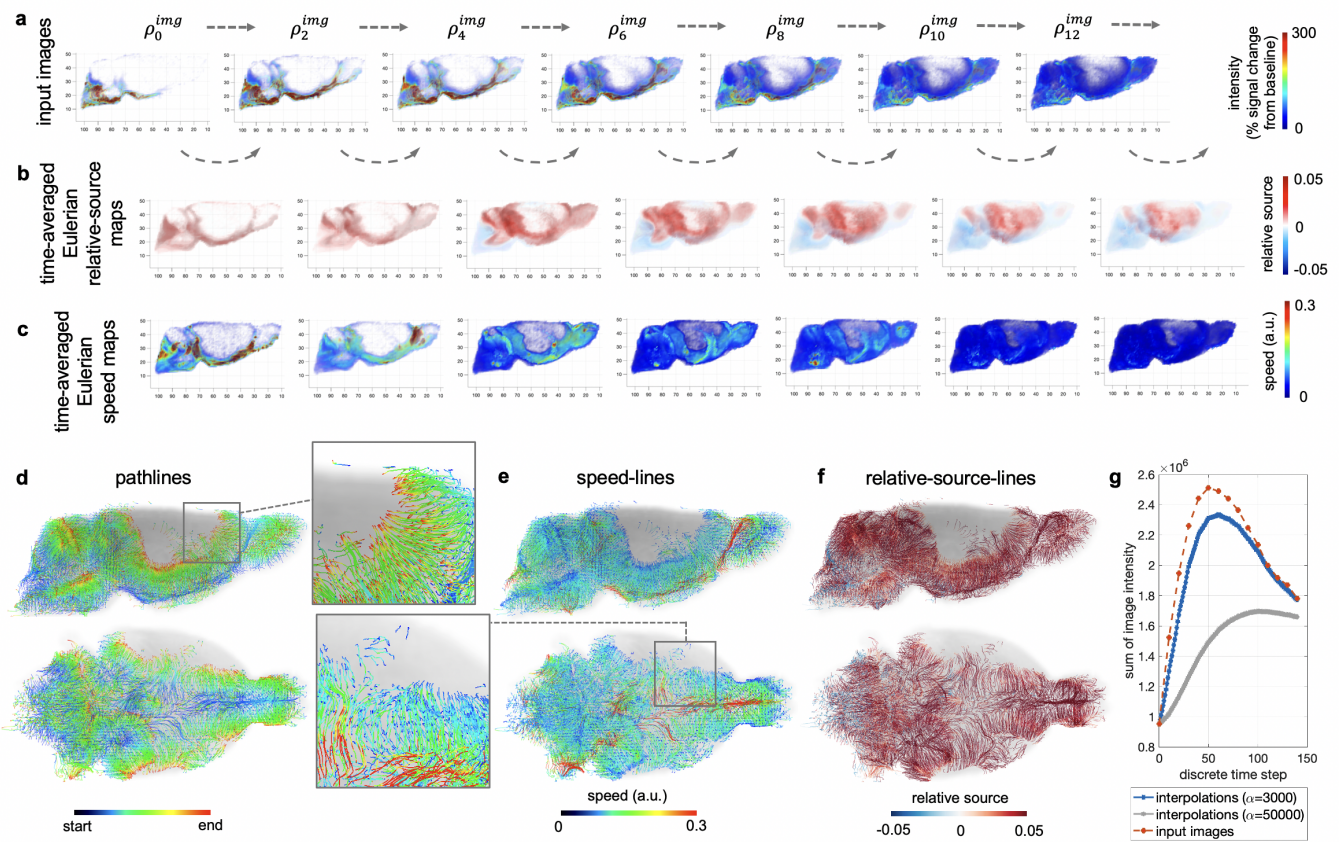


Fig. 2. 3D Rat Brain: **a:** Rat brain MRIs, shown in 3D rendering and from the right-lateral view, were put successively into the urOMT algorithm. **b-c:** As returned outputs, the Eulerian time-averaged relative-source maps and speed maps between every other image were plotted in 3D rendering and shown from right-lateral view, indicating the mass gains/loss and speed distribution over time, respectively. **d-f:** Under Lagrangian coordinates, pathlines, color-coded with start and end points, show the trajectories of the solutes/tracers in brain starting at $t = 0$. The speed-lines show the speed values along pathlines, and similarly relative-source-lines show the mass gains or loss along pathlines. All lines are shown from both the right-lateral and bottom views. **g:** The total image intensity of input MRIs and returned interpolations at different values of model parameter α are compared over time.

- [4] Xinan Chen, Anh Phong Tran, Rena Elkin, Helene Benveniste, and Allen R. Tannenbaum. Visualizing fluid flows via regularized optimal mass transport with applications to neuroscience, 2022.
- [5] Yongxin Chen, Tryphon T Georgiou, and Michele Pavon. On the relation between optimal transport and Schrödinger bridges: A stochastic control viewpoint. *Journal of Optimization Theory and Applications*, 169(2):671–691, 2016.
- [6] Yongxin Chen, Tryphon T Georgiou, and Allen Tannenbaum. Interpolation of density matrices and matrix-valued measures: The unbalanced case. *Euro. Jnl of Applied Mathematics*, 30(3):458–480, 2018.
- [7] Lenaic Chizat, Gabriel Peyré, Bernhard Schmitzer, and François-Xavier Vialard. Scaling algorithms for unbalanced optimal transport problems. *Mathematics of Computation*, 87(314):2563–2609, 2018.
- [8] Marco Cuturi. Sinkhorn distances: Lightspeed computation of optimal transport. In *Advances in neural information processing systems*, pages 2292–2300, 2013.
- [9] Thomas Gallouët, Maxime Laborde, and Léonard Monsaingeon. An unbalanced optimal transport splitting scheme for general advection-reaction-diffusion problems, 2017.
- [10] Leonid V Kantorovich. On a problem of monge. *CR (Doklady) Acad. Sci. URSS (NS)*, 3:225–226, 1948.
- [11] Sunil Koundal et al. Optimal mass transport with lagrangian workflow reveals advective and diffusion driven solute transport in the glymphatic system. *Scientific Reports*, 10, 2020.
- [12] Damiano Lombardi and Emmanuel Maitre. Eulerian models and algorithms for unbalanced optimal transport. *ESAIM: Mathematical Modelling and Numerical Analysis*, 49(6):1717–1744, 2015.
- [13] Jan Maas, Martin Rumpf, Carola Schönlieb, and Stefan Simon. A generalized model for optimal transport of images including dissipation and density modulation, 2015.
- [14] Gaspard Monge. Mémoire sur la théorie des déblais et des remblais. *Histoire de l'Académie Royale des Sciences de Paris*, 1781.
- [15] Cédric Villani. *Topics in Optimal Transportation*. American Mathematical Soc., 2003.
- [16] Cédric Villani. *Optimal Transport: Old and New*, volume 338. Springer Science & Business Media, 2008.